MOTION AND METAL ARTIFACT CORRECTION FOR ENHANCING PLAQUE VISUALIZATION IN CORONARY COMPUTED TOMOGRAPHY ANGIOGRAPHY

by
Xiaoxuan Zhang

A thesis submitted to Johns Hopkins University in conformity with the requirements for the degree of Master of Science in Engineering

Baltimore, Maryland
July, 2016

Abstract

Atherosclerosis detection remains challenging in coronary CT angiography due to motion and metal artifacts. Motion artifacts arising from rapid coronary artery displacement occurred over the acquisition window may lead to intensity reduction and feature doubling or distortion, severely hindering the visualization of a plaque of interest. Similarly, for patients with cardiac implants, pacing electrodes or implant lead components can create substantial blooming and streak artifacts in the heart region, obscuring the background anatomy adjacent to the component. In this work we presented an image-based compensation framework exploiting a rigid and linear motion model for correcting motion artifacts, and a novel reconstruction method incorporating a deformable model for metal leads to eliminate metal artifacts to improve plaque visualization. The feasibility of both correction methods is validated with simulation and experimental studies. We found a dramatic improvement in the ability to visualize fine details in the coronary artery plaque after the application of the proposed motion compensation method. Similarly, anatomy visualization even near the boundary of the component has greatly improved after reconstruction with the deformable known-component model. Both proposed methods have the potential to improve plaque visualization and characterization in coronary CT angiography.

Thesis Committee

J. Webster Stayman

Assistant Professor, Department of Biomedical Engineering

Elliot R. McVeigh

Adjunct PT Professor, Department of Biomedical Engineering

Daniel Herzka

Assistant Assistant Professor, Department of Biomedical Engineering

Acknowledgements

I would like to thank my supervisors and mentors Dr. Elliot McVeigh and Dr. J. Webster Stayman for their continuous support of my research study. Their immense knowledge has helped me in solving difficulty puzzles and achieving many of my goals, and their patience and motivation has encouraged me to keep learning and improving. I also want to thank them for being in my thesis committee, along with Dr. Daniel Herzka, for their positive feedback and comments.

In addition, I would like to thank my labmates Dr. Grace Jianan Gang, Dr. Aswin Mathews, Dr. Hao Zhang, Mr. Steve Tilley II for their guidance and insightful discussions on research projects, which has inspired me to develop effective solutions and overcoming challenges. Special thank you goes to Dr. Gang and Mr. Ali Uneri, for their generosity in spending enormous time on answering my questions and walking me through solving technical issues.

I would like to thank Dr. Elizabeth Logsdon for her invitation to me for being a teaching assistant of the Biomedical Engineering Practice and Innovation summer course. I was able to learn about cutting-edge technologies outside of my research work and witness how they were applied to solve urgent medical problems.

Last but not least, I would like to thank my parents, Mr. Minghao Zhang and Mrs. Weitao Huang, for their love and understanding. They have always been there for me in my hardest times, and encourage me to make my own decisions and be persistence. I also want to thank Mr. Dengrong Jiang for being my significant other and taking care of me even at his most stressful times.

Table of Contents

List of Figures

List of Tables

I. Introduction

Patients with atherosclerotic plaques, or lesions formed from buildup of lipid, calcium, and fibrous tissue at the coronary arterial wall, may benefit from coronary computed tomography angiography (CCTA), a non-invasive imaging technique that has short scanning time and high spatial resolution. This method may be particularly useful for those with metallic cardiac implants, including pacemakers and cardioverter defibrillators, due to its lack of contraindication to metal. In addition to atherosclerosis, CT angiography may also permit detection of complications associated with implantable devices such as lead perforation. Yet these tasks remain challenging owing to artifacts caused by coronary artery motion as well as those from metal devices. Acquiring motion-artifact-free images is not a trivial task given the rapid arterial motion (up to 65 mm/s when HR < 60 bpm [1]), or when the patient has irregular cardiac rhythm. When acquired at the wrong cardiac phase, images are uninterpretable. Manifest motion artifacts often seen are intensity lowering, feature doubling, blurring, and distortion. Furthermore, up to 60% of images are significantly degraded by metal artifacts resulting from endocardial leads, which prevents reliable coronary artery assessment. Streaks and blooming around metal components can largely obscure the surrounding anatomy, making it difficult to visualize detailed features of interest.

An extensive number of correction methods for motion artifacts have been reported. Solutions widely utilized for cardiac motion correction involve hardware, beta-blockers, and multisector algorithms [2]. Yet development of imaging hardware such as multi-detector and dual-source systems [3], [4] is expensive and has physical limitations. Beta-blockers have limited efficacy in controlling heart rate [5], and they cannot be administered on patients with contraindications. Multisector methods [6], [7] involve acquisition of multiple heartbeats that increases patient dose and fail when the cardiac motion is not repeatable. Contrarily, motion

estimation and compensation methods leveraging reconstruction images [8], [9] are proven to be effective in mitigating motion artifacts as well as very cost-efficient, yet they either rely on the presence of at least one static reference image or 4D datasets for tracking and interpolating cardiac motion. In this work, we propose a purely image-based iterative motion estimation strategy exploiting a 3 degree-of-freedom (DoF) motion model and anatomical features associated with an object of interest. We presume that locally the motion is rigid and linear over the acquisition window in diastasis [10], [11], and severe artifacts predominantly result from translational coronary artery motion. No initial motion estimations are required, and dimension of the motion estimation is significantly reduced with these presumptions.

Similarly, numerous metal artifact correction methods have been proposed. One idea that arises is to replace low-fidelity data correspond to the metal components through interpolation [12]–[14], in-painting [15], [16], and many other similar approaches [17], [18]. Improvement on the overall image quality is achievable with these methods. Yet features that are in close proximity to the object, which may often be the object of clinical interest (i.e. plaques, fractures), remain unseen or obscure due to residual artifacts at the at the component edges. Recently, the class of known-component reconstruction (KCR) [19]–[21] has demonstrated significant metal artifact correction even at the boundary of the component. Such performance is achieved through integration of models of metal components into the reconstruction process, in which each model is constructed based on specific component configuration and material composition. Yet such information of components might not be available, and it is possible for components to undergo deformation during or after surgical placements. Further metal artifact reduction may be obtained through an additional integration of a polyenergetic x-ray system model into the estimation as well as scatter correction. Therefore, we proposed a reconstruction framework including three stages: 1) modeling of a

specific component in the reconstruction field-of-view in which the model parameterization enables deformation within a constrained volume, 2) jointly optimizing model and registration parameters, and 3) scatter correction and deformable known-component model-based reconstruction.

II. Methods

A. Motion Artifact Correction

1. Image-Based Motion Compensation

The proposed motion compensation framework is shown in Figure 1. A standard FBP reconstruction is performed using the projection data. This reconstruction is uncompensated and may contain an object of interest that is degraded by motion artifacts. A volume of interest (VoI) containing the object is then selected. Our presumption is that the motion is rigid and linear within this small VoI, regardless of the complex gross cardiac motion. In addition, artifacts predominantly arise from translational coronary artery motion, and thus rotational motion may be neglected. Consequently, we proposed a motion model describing a 3 DoF rigid transformation of the VoI, which requires only 3 parameters defining the relative displacement of the volume over the acquisition window [10], [11]. The transformation for each projection view is interpolated from these 3 parameters. The resulting transformations make up of a specific motion trajectory which is applied to the backprojection process for reconstructing the selected VoI. Defined in Equation 2, the negative gradient magnitude of the reconstructed volume serves as a metric for evaluating the compensation effectiveness introduced by the current trajectory. A non-linear, non-convex optimization algorithm, the

Covariance Matrix Adaptation Evolution Strategy (CMA-ES), is employed to search for the motion trajectory that minimizes the metric. The objective function is shown as:

$$\hat{T} = \arg\min_{T} G(T, \mu) \tag{1}$$

$$G(T, \mu) = -\sum_{j} \nabla_x \mu_j^2 + \nabla_y \mu_j^2 + \nabla_z \mu_j^2 \tag{2}$$

where the negative gradient magnitude G of the reconstructed volume of interest μ is evaluated through summing the directional gradient of each voxel j for the current motion trajectory T. The gradient operator is denoted by ∇ and the subscript describes the corresponding orthogonal direction of the volume.

2. Simulation Methods

To test the feasibility of the proposed motion compensation framework, we designed a digital coronary artery tree phantom containing three arterial branches with varying diameters, and randomly add high contrast, irregular-shaped objects to the inner wall of each branch. The digital phantom is then forward projected using a curved detector operator and a known motion trajectory is applied on the phantom during the process. 800 projections are generated over 360° and each has a size of 896 bins x 240 rows, with 1 mm^2 pixel spacing. A standard FBP reconstruction is performed using the motion contaminated projections for the volume of interest selection. The proposed algorithm is then applied on the selected volume. A static reconstruction volume is also obtained from motion free projections, serving as a reference image for evaluating the motion-compensated reconstruction.

We chose a translation of 6, 4, 8 mm in the positive x, y, and z direction respectively as the simulated motion. The amplitude is determined based on statistics reported by Lu et al. [22] and displacements of coronary artery branches quantified from patient CCTA data. The

quantification algorithm is described as follows. First we select the motion-artifact-free image volumes through visual assessment. That is, the data happen to be taken at the quiescent periods of the cardiac cycle. Normally the quiescent periods are the end systolic (ES) and the end diastolic (ED) phase, but these periods may shorten or disappear as heart rate increases. In addition, different coronary artery branches have quiescent periods at different time points of the R-R interval, and thus we have identified not only different quiescent periods between patients, but also different quiescent periods between branches (RCA vs. LCA) within the same patient. We then performed a coronary artery centerline extraction method reported by Friman et al. [23], the winning algorithm of the second MICCAI grand challenge. The method is implemented using MeVisLab, which is a graphical programming software free to the public. By labeling artery of interest with a few seed points, we would be able to obtain a branch centerline (see Figure 2 and Figure 3). To simplify the displacement quantification and ensure measurement accuracy, only the bifurcation points of the artery tree were used for displacement calculation.

3. Experimental Methods

We further validated the feasibility of the algorithm with experimental data acquired on a CBCT testbench (shown in Figure 4). A cadaveric heart sample containing distorted arteries and irregular-shape calcification pieces was chosen as the imaging object. We first obtained and reconstructed the standard motion-free projections of the sample to identify features of interest. The static volume would serve as a reference image for the performance evaluation. In addition, we employed a 6-axis positioner that can generate motion during data acquisition. Specifically, translational motion of approximately 8 mm was introduced to the sample in the superior-inferior direction. The X-ray tube is operated at 80 kVp (+1 mm Al,

0.5 mm Cu) and the dose is 0.8 mAs per projection. 720 projections (1536x1536 pixels, 0.278 mm^2 spacing) are acquired over 360°. The reconstruction volume has size of 45x45x1.5 mm with 0.15 mm^3 voxels. For the optimization, we specify boundary constraints to be less than 15 mm for the amplitude of motion in each dimension, and convergence criteria is achieved when change in best solution is less than 10^{-2}. Runtime of this algorithm is up to 30 minutes.

B. Metal Artifact Correction

1. Polyenergetic Known-Component Reconstruction Overview

The core of the Poly-KCR approach is a mixed fidelity model, which combines the unknown anatomical structures and a deformable homogeneous component. This model may be written as

$$\mu = \mu_* + T\mu_I \tag{3}$$

in which μ_* denotes the background anatomy and μ_I represents the component. The transformation T is the outcome of a preregistration process, in which the component is registered to the reconstruction volume while undergoing deformation. Based on the mixed fidelity model, the associated forward model may be derived as:

$$\bar{y} = \mathbf{D}\{g\}\exp(-\mathbf{A}\mu_*) * f(-\mathbf{A}\mu_I) \tag{4}$$

in which $\mathbf{D}\{g\}$ is a diagonal matrix forming from the vector g, which denotes the system gain. The forward model for the anatomical background, $\exp(-\mathbf{A}\mu_*)$, is modified upon the Beer's Law. At this step, we seek to model the process of x-ray emitting from the source, penetrating the object, and ultimately interacting with the detector. And in this case, the projection operation has to be a discrete-to-discrete conversion, since image volume is parameterized using voxels and the detector is composed of a finite number of detector elements. Therefore,

in this model, the system matrix $\mathbf{A}$, which specifies the contribution of a particular voxel to a particular measurement, is adopted. This forward model assumes single-energy x-ray photon emission, or a monoenergetic beam.

On the other hand, although a system matrix $\mathbf{A}$ is also utilized in the forward model for the metal component, $f(-\mathbf{A}\mu_I)$, this model assumes polyenergetic beam and has much higher fidelity, aiming at eliminating artifacts associated with the component such as streaks and "blooming". We denote this novel forward model as the *spectral transfer function* (STF), which approximates polyenergetic beam by specifying a polynomial relationship between x-ray pathlengths and the measurements [24]. This relationship is defined as:

$$f(p;\kappa) = \exp\left(\sum_{k=1}^{K} \kappa_k (p)^k\right) \tag{5}$$

where p denotes x-ray pathlength through the component and κ depends on the component material and the x-ray beam spectrum. When $\kappa_k \equiv 0$ for all $k \neq 1$, the above equation may be used to approximate a monoenergetic x-ray system, and therefore κ_k is the negative attenuation coefficient of the component. As the order of the polynomial k increases to second or third, the function becomes sufficient to model the attenuation behavior of the component.

With the mixed fidelity model, we may jointly estimate background attenuation and STF coefficients given the measurements by using the following reconstruction objective function:

$$\{\hat{\mu}_*, \hat{\kappa}\} = \operatorname{argmin} \Phi(\mu_*, \kappa; y) = \operatorname{argmin} L(\mu_*, \kappa; y) - \beta R(\mu_*) \tag{6}$$

By applying a log transform on the mixed fidelity model, we may derive the negative log-likelihood equation, which is a weighted 2-norm including the monoenergetic forward model

of the anatomical background, the polyenergetic model of the component, and the normalized and log-processed projection data:

$$L(\mu_*, \kappa; y) = \left\| \mathbf{A}\mu_* - \sum_{k=1}^{K} \kappa_k(p)^k - \log(\mathbf{D}\{g\} * \bar{y}^{-1}) \right\|_W^2 \quad (7)$$

One thing to note is that in standard filtered backprojection, the tradeoff between image noise and spatial resolution is controlled by manipulating Hanning filters and a cutoff frequency (as a fraction of the Nyquist rate). The effectiveness of the filter drops to zero beyond the cutoff frequency, and hence the lower the cutoff frequency, the lower the image variance, and the smoother the image appears.

In penalized likelihood reconstruction, the noise-resolution tradeoff is achieved with a different set of methods, involving regularization terms and parameters. Regularization term refers to the type of regularizers one would like to use, and the regularization parameter is for controlling the strength of the regularization. One typical penalty function is quadratic penalty, which tends to enforce smoothness through the entire image to achieve good noise reduction:

$$R(\mu) = \sum_j \sum_{k \in N} w_{jk} \psi(\mu_j - \mu_k) \quad (8)$$

where N denotes the neighboring voxels of voxel j and ψ is a convex function that enforce neighboring value similarity [25]. Quadratic penalty might be undesired since it also penalizes edges in the image, and thus non-quadratic regularizations such as Lange or P-Norm penalty serves as a better term in this case, given the fact that it decreases the penalty on increasing voxel differences and thus preserve true edges while reduce noise.

In this study, we employed a non-quadratic regularization term combing the basic quadratic penalty with an edge-preserving penalty function named the Huber function [26]:

$$\psi_H(x) = \begin{cases} \frac{1}{2\delta}x^2, & |x| \leq \delta \\ |x| - \frac{\delta}{2}, & |x| > \delta \end{cases} \quad (9)$$

where the term δ controls the application range of the two functions. The quadratic penalty will be applied to differences smaller than δ whereas those the edge-preserving penalty to those greater than δ. When δ approaches zero, the quadratic penalty term is eliminated and the image appears to be "cartoonish", or piecewise-constant. When a large δ is chosen, the regularization predominantly results from the basic quadratic penalty, with an exact difference of a factor of $1/\delta$.

2. Model Parameterization and Preregistration of Deformable Known Component

As mentioned above, prior to the application of Poly-KCR to the CT angiogram target, the component has to be preregistered to the reconstruction volume. In other words, the transformation T has to be determined before the reconstruction process. A model for the wire-like components including pacing leads or implantable cardioverter defibrillator, which is μ_I in Equation 3, is essential for the preregistration step. Although it is easy to obtain morphological information of the implant, the leads are flexible and can deform when inserted into the heart through a vein. This deformation is often unknown and varied from patient to patient. Inspired by Stayman et al. [27], we proposed a novel parameterization technique for modeling wire-shape components using a spline curve with control points defining its shape and an additional parameter defining the radius of the solid wire.

An overview of the parameterization process is shown in Figure 5. To ensure the modeling accuracy and reduce the parameterization complexity, a rectangular volume containing an initial wire model is segmented out from a standard FBP reconstruction volume

using the Otsu's method [28]. The volume is binary and any voxel within the wire has a value of 1. The wire centerline is composed of the centroids of the axial slices of the segmented wire, and the control points are sampled from these centroids and spaced out evenly along the centerline. Differed from the conventional control point definition where only the end points are on the curve and the rest are nearby for controlling the shape, our definition of control points is more intuitive and can ease the process of inducing exact deformations on the model. This step will also facilitate the model refinement process, which is to constrain the wire volume within the specified wire radius. To obtain a refined wire volume, we can simply compute the minimal distance of each voxel within the binary volume to the centerline of the wire, and the ones with minimal distance less than the specified radius are set to 1, otherwise 0.

Although this refinement approach is intuitive and accurate, it is time-consuming. Yet improving this process is possible because the refined volume is indeed very sparse. Therefore, we presume that the refined wire model will be within a constrained volume, which is a dilated version of the segmented wire, and only voxels within the dilated model have the potential to be voxels within the refined model. That is, voxels outside the dilated wire will always have the value of 0, and the minimal distance computation and comparison will only be carried out for the voxels within the dilated wire volume. The extend of the dilation is set to be large enough to not only accommodate potential morphological deformation but also unknown translational and rotational motion. This general deformable model can represent a good amount of wire-shaped components and it is relatively easy and fast to implement. Combination of the deformable model and the Poly-KCR method is referred as Poly-dKCR.

This Poly-dKCR method is a staged process where registration of the component model is performed prior to the reconstruction. This manner hence enables the usage of any

registration method of choice. In this study, we proposed a 3D-2D registration method improved upon an algorithm developed by Otake et al. [29] for our purposes, since we have already acquired 2D projection data of the component with anatomical background and established a model of the wire-shape component in the previous step.

The proposed registration method is illustrated in Figure 6**Error! Reference source not found.**. Our goal is to jointly estimate the morphological and transformational parameters of the 3D wire-shape model, which are presented using d and T, respectively. The morphological parameters are the control point locations and the wire radius. The transformation is essentially a vector containing six-variable vector defining the object's translational and rotational motion, including surge t_x, sway t_y, heave t_z, pitch θ_x, roll θ_y, and yaw θ_z. Projections of a deformed wire-shape model with one transformation applied is generated using a forward projector. The gradient correlation between the acquired projection data containing both the component and the anatomy and the projection of the model is computed for each view to quantitatively evaluate image similarity. A non-convex, non-linear optimization algorithm called Covariance Matrix Adaptation Evolution Strategy (CMA-ES) is employed to search for the model parameters that maximize the total gradient correlation metric computed using all the projections. We employed the following objective function:

$$\{\hat{d}, \hat{T}\} = \arg\max_{d,T} \sum_{\theta} GC\left(y'_{\theta}\left(T\mu_I(d)\right), y_{\theta}\right) \tag{10}$$

$$GC(y', y) = \frac{1}{2}\Big(CC(\nabla_x y', \nabla_x y) + CC\left(\nabla_y y', \nabla_y y\right)\Big) \tag{11}$$

$$CC(y', y) = \frac{\sum_{i,j}\left(y'_{i,j} - \bar{y}'\right)\left(y_{i,j} - \bar{y}\right)}{\sqrt{\sum_{i,j}\left(y'_{i,j} - \bar{y}'\right)^2}\sqrt{\sum_{i,j}\left(y_{i,j} - \bar{y}\right)^2}} \tag{12}$$

where GC denotes the gradient correlation between model projection data and true measurements [30]. Derivation of the gradient correlation builds upon the normalized cross correlation (CC), and it takes the two directional gradients of each projection data as the inputs. Additionally, x and y represent the horizontal and vertical direction of the 2D image, and i, j is the pixel coordinates within a projection.

While morphological parameters of the model have been pre-determined in the model refinement process and are fed to the optimization algorithm as part of the initialization, the process does not require initial guesses of the tran which ational parameters. Meanwhile, the morphological changes of the model are constrained by the dilated volume, given the presumption that only voxels within this volume have the possibility to be those within the optimized wire volume.

3. Experimental Methods

To verify the feasibility of the proposed method, we designed a cardiac phantom (shown in Figure 7) and obtained physical measurements using a CBCT test bench (shown in Figure 8). This phantom is built to emulate the situation when an object of interest, such as a calcified plaque, is located within close proximity to a metal component. A 1.59 mm Teflon sphere, which has Hounsfield unit attenuation similar to bone structure, is glued to the inner wall of a long, transparent vinyl tube. The vinyl tube is filled with distilled water and is encapsulating a bare copper wire mimicking a pacing lead.

Projection data of the customized cardiac phantom is obtained on the test bench using a system geometry similar to a clinical cardiac scan. 360 projections are acquired covering 360° using a flat panel detector (PaxScan 4030CB, Varian Medical Systems, Palo Alto CA) and each projection has 1536x1536 pixels at 0.278 mm pixel pitch. The source-to-detector distance

(SDD) is set to be ~1100 cm and the source-to-axis distance (SAD) is ~850 cm. The x-ray tube is operated at 80 kVp with 1 mm Aluminum and 0.5 mm copper filtration, and the amount of dose is 1.6 mAs per frame.

A standard FBP reconstruction of size 650x700x305 voxels with 0.5 mm^3 spacing, filtered by a Hann function combined with a cutoff frequency at 20% of Nyquist frequency, can be obtained from the projections. This reconstruction is used for obtaining the segmented component volume and for determining the parameters, which initializes the preregistration process. At each iteration of the preregistration, 80 candidate model volumes with distinct morphological and transformational parameters are evaluated and 100 iterations are needed for the algorithm to converge. After obtaining the optimal model parameters, a scatter correction method is applied on the projection data. The scatter is empirically estimated with the pixel values within and adjacent to the component and represented as a sinusoidal function of rotation angle. Specifically, a constant defined by the function is subtracted from the corresponding projection acquired at the same rotation angle. The proposed Poly-dKCR method is then performed using the model parameters and the scatter corrected projections. An aforementioned non-quadratic penalty is employed ($\delta = 10^{-4}$) and the regularization strength is set to be $\beta = 0.05$. In total, 40 separable quadratic surrogates with 20 ordered-subsets are utilized.

III. Results

A. Coronary Artery Motion Quantification and Compensation

The outcome of the coronary artery motion quantification strategy is shown in the tables below. Table 1 listed the locations of bifurcation points at various coronary artery

segments. The labels are assigned according to the ACC/AHA 29-segment guidelines [31]. Since coronary artery structure varies largely among the population, we created our own version of segments based on the acquired patient data (see Figure 9 and Figure 10). The major difference lies in the right coronary artery, where the conus branch and the sinus node artery are included. Based on the modified segment map, we are able to label the extracted bifurcation points by their physical locations. For instance, at 30% of the R-R interval shown in Table 1, the first bifurcation is connecting the left circumflex artery segment and the first obtuse marginal branch segment, which is referred as LCX_OM1. The corresponding three-dimensional coordinates of the bifurcation are also measured and reported. These coordinates are derived using the image slice numbers reported by OsiriX (Pixmeo SARL). The same convention applies to the bifurcation points extracted at the end diastolic phase (Table 2). One thing is note is that the point numbers are randomly assigned, only the physical locations are used for finding the same point at different phases. The displacements are then obtained by computing the location difference of the same point, and the results are shown in Table 3.

The performance of the proposed motion compensation strategy based on the simulation and experimental studies are also reported below. For the simulation study, an axial slice of a standard FBP reconstruction of the digital coronary artery tree phantom, highlighted with yellow border, is shown in Figure 11. Two high-contrast, irregular-shaped objects are also shown. The motion-contaminated reconstruction is highlighted with red border. We are able to generate typical motion artifacts that are often seen in patient CCTA images, including shading near the boundaries, blurred targets, and distortion of coronary arteries. After applying the compensation algorithm, we obtain a compensated volume in which the motion artifacts are mitigated (highlighted with blue border). The artery boundaries as well as the calcifications are visible and qualified for quantitative assessment. In addition to visual assessment, the

performance of the algorithm is quantified with two image similarity metrics, the structural similarity index [32] and the root mean square error:

$$SSIM(x,y) = \frac{(2\mu_x\mu_y)(2\sigma_{xy})}{(\mu_x^2+\mu_y^2)(\sigma_x^2+\sigma_y^2)} \tag{13}$$

$$RMSE(x,y) = \sqrt{\frac{1}{n}\sum_{i=1}^{n}(x_i-y_i)^2} \tag{14}$$

The results of the simulation study are shown in Figure 12. Image similarity increases by approximately 25% after applying the compensation on the selected volume of interest, and the compensated volume is nearly the same as the reference.

The results of the experimental study are consistent with the simulation outcomes. We identified a piece of calcium in the explanted heart sample, and due to motion artifacts, its shape and size are uninterpretable. Note that the soft-tissue boundaries adjacent to the calcium have also disappeared. Detailed structures of the calcium are visible in the compensated image, and the tissue boundaries are not only recovered, but also sharper than the ones in the reference image. The motion compensation method may potentially correct artifacts resulting from erroneous geometry calibration.

B. Poly-KCR Method with Deformable Model

The qualitative performance of the Poly-dKCR method is shown in Figure 15. The obtained reconstruction (Figure 15B) is displayed adjacent to the FBP reconstruction (Figure 15A). The outcome of the preregistration is shown using a red overlay, which represents the wire-like implant model. It is apparent that the streak artifacts presented at the wire boundaries in the FBP reconstruction are significantly reduced after applying the Poly-dKCR method, and

thus we can have good visualization of the Teflon sphere. Shading artifacts are suppressed in the Poly-dKCR reconstruction and therefore the attenuation homogeneity in the central region of the tube has greatly enhanced. Recall that the tube is filled with water, which have an attenuation value close to that of the cardiac phantom.

We have also performed a quantitative assessment of the method by measuring the peak attenuation coefficient of the Teflon sphere. The improvement provided by Poly-dKCR is significant. We expect the attenuation value of Teflon to be 0.414 mm^{-1} given an effective energy of 60 keV and material density of 2.2 g/cm^3. The peak attenuation coefficient of the sphere in the FBP reconstruction is 0.0195 mm^{-1}, which is significantly lower than the expectation. On the other hand, the value measured in the Poly-dKCR volume is 0.0408 mm^{-1}, which doubles the FBP value and closely approximated the expected attenuation.

IV. Conclusions and Future Work

We developed and evaluated an image-based motion compensation framework that exploits a rigid and linear motion model emulating local residual cardiac motion. Motion trajectory of a selected volume of interest is estimated through maximizing sharpness of the reconstruction image with the non-convex CMA-ES method, and no initial motion estimates are required. The feasibility of the proposed method is validated with both simulation and experimental studies. A dramatic improvement in the ability to visualize fine details in the coronary artery plaque suggesting great potential for clinical application. Potential future work involves developing more sophisticated and complex simulation and experimental methods and applying such method on patient data.

Additionally, we proposed and evaluated a novel polyenergetic reconstruction method involving a deformable model for wire-like cardiac implants. Prior to the reconstruction is a

gradient-based registration method that estimated the morphological and transformational parameters of the implant. The optimized model is then integrated into the polyenergetic known component reconstruction process which further estimates the spectral parameters associated with the component. Resulting images are nearly artifact-free, permitting good visualization of Teflon target as well as the anatomical background. Next step of the study may include application on phantom data with metal implants of different configurations, and target objects with varying attenuation coefficient values. In conclusion, we proposed two strategies aiming at overcoming the major challenges – motion and metal artifacts in coronary CT angiography, and positive performance of the proposed methods shows the potential to enhance visualization and diagnosis of atherosclerotic plaque and calcification.

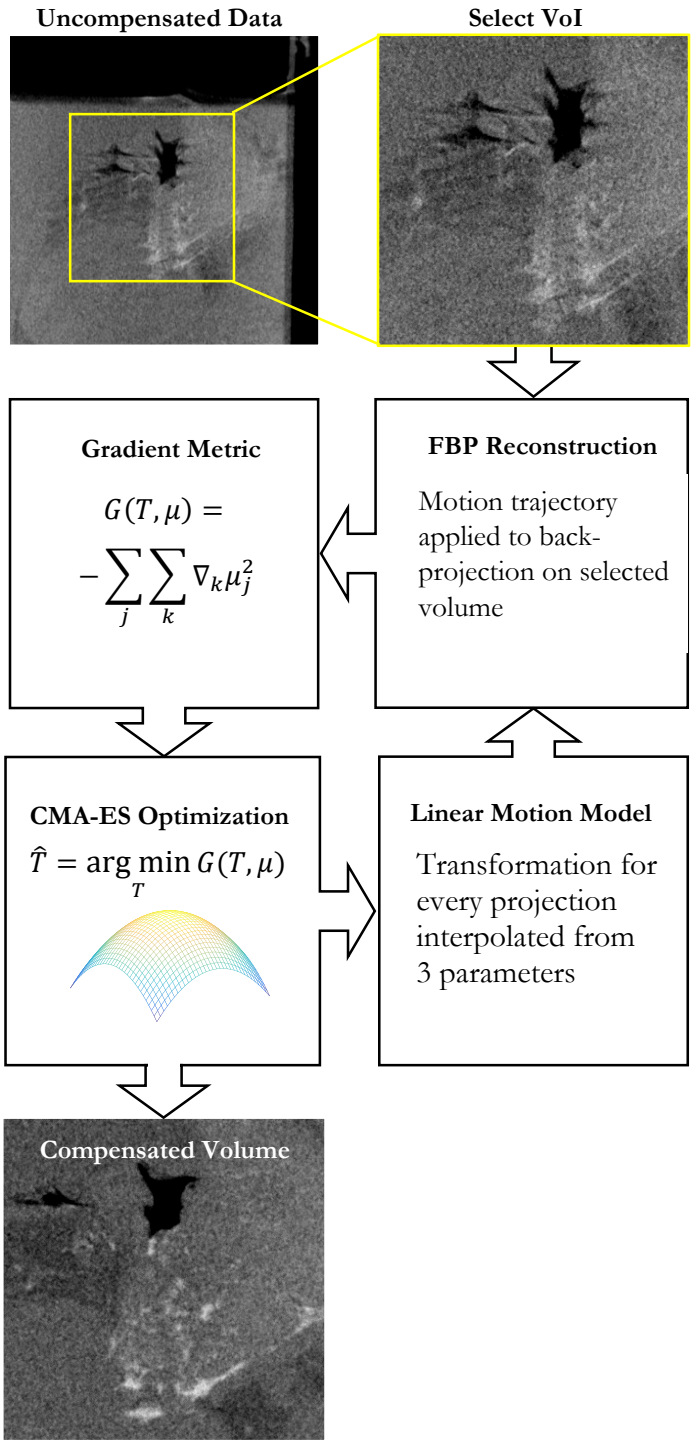

Figure 1. A flowchart of the image-based motion estimation and compensation method.

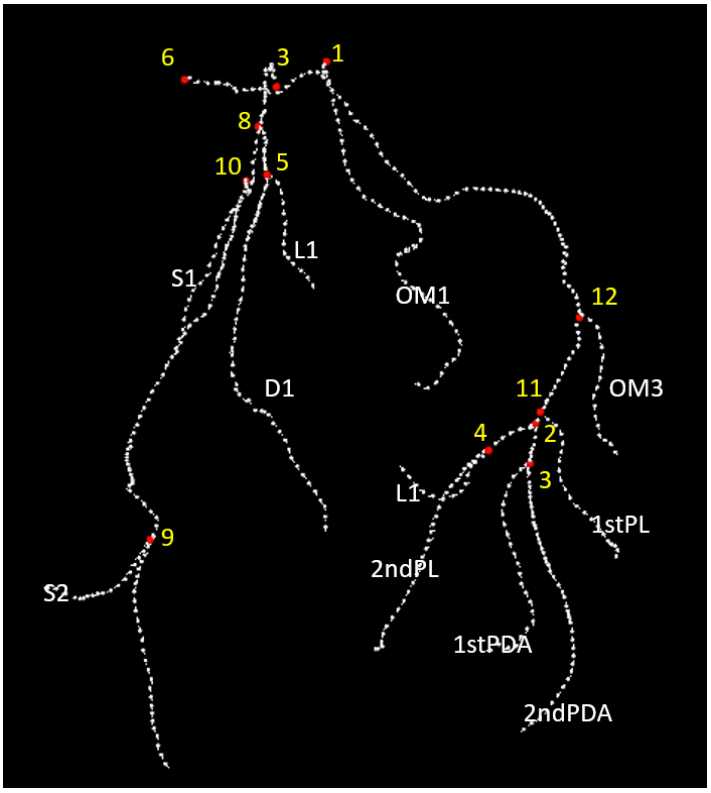

Figure 2. Coronary artery tree centerline extraction at end systolic phase.

Each bifurcation point is labeled with numbers and coronary artery segmented are labeled based on the AHA standard.

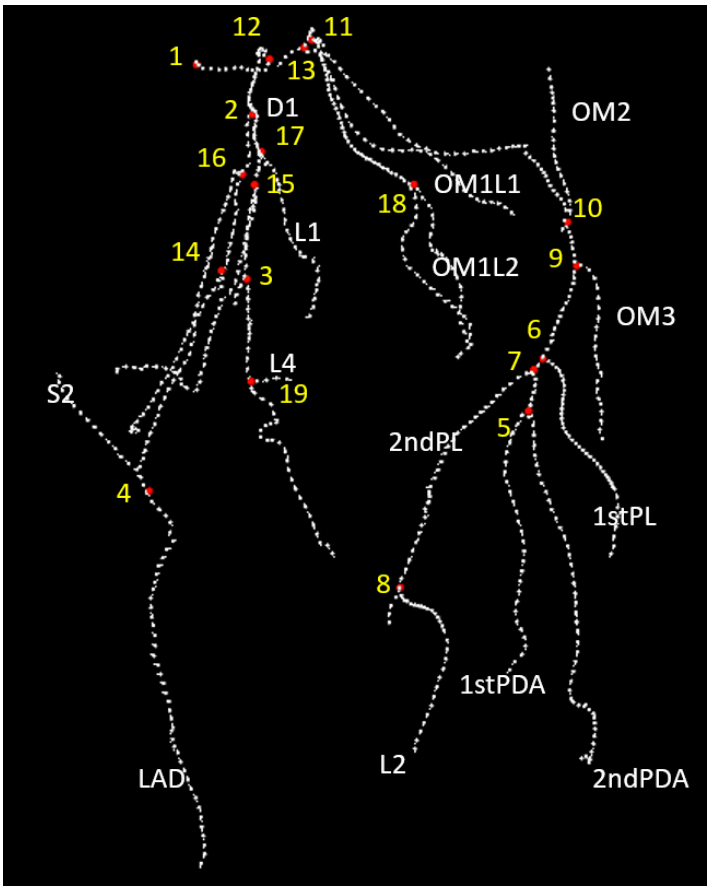

Figure 3. Coronary artery tree centerline extraction at end diastolic phase.

Although the bifurcation points are labeled with numbers, it does not correspond to the numbers in the end systolic phase. Matching bifurcation points are determined based on the anatomical position on the coronary artery tree.

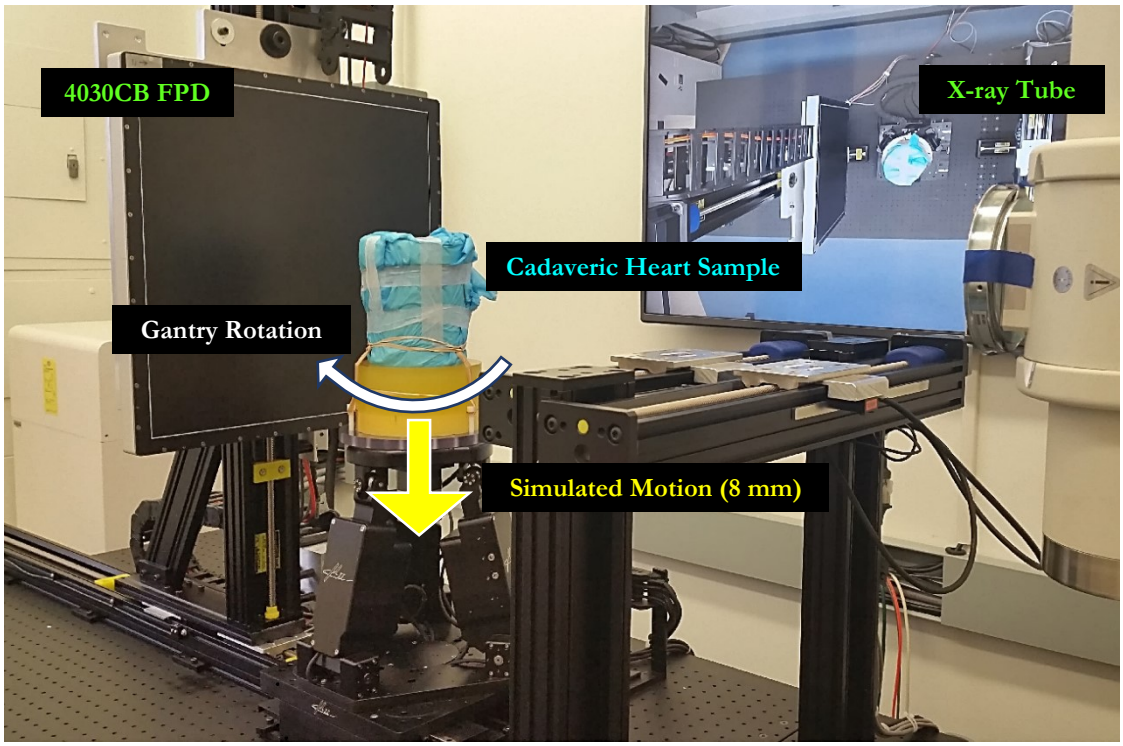

Figure 4. Motion Compensation in experimental testbench data (human heart).

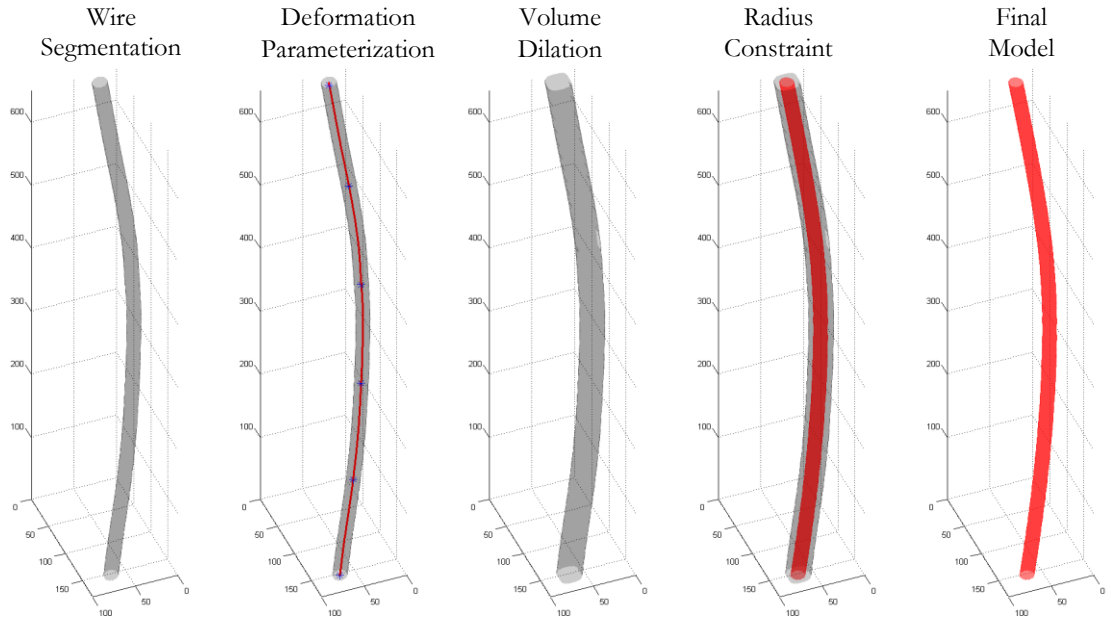

Figure 5. Overview of the implant model parameterization that includes morphological and transformational variables

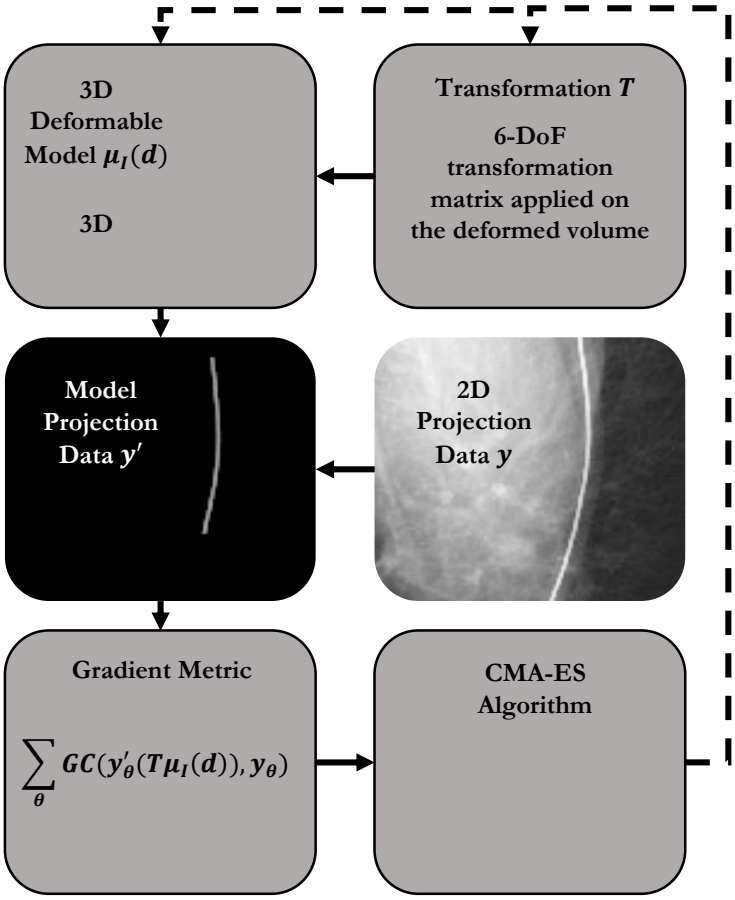

Figure 6. Flow diagram of the iterative gradient-based preregistration process.

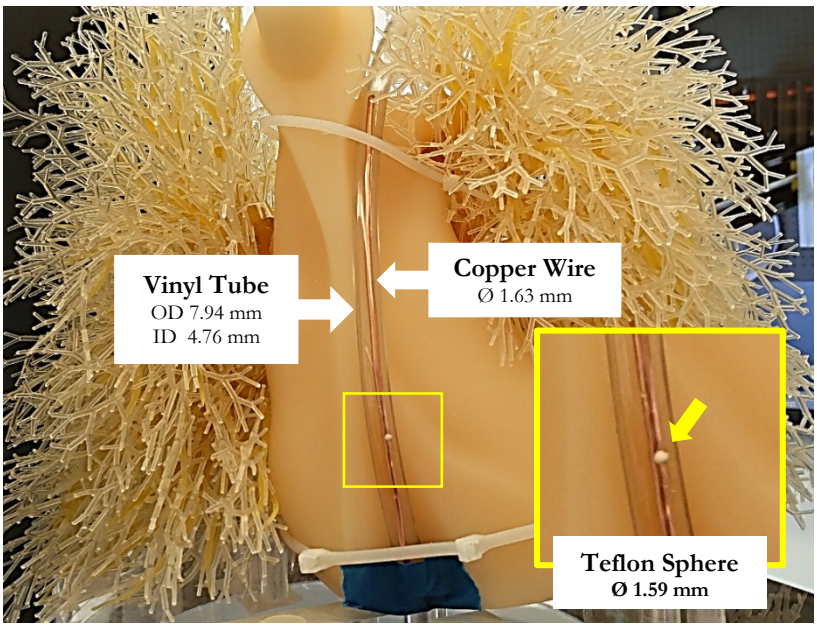

Figure 7. Cardiac Phantom with catheter and a plaque of interest

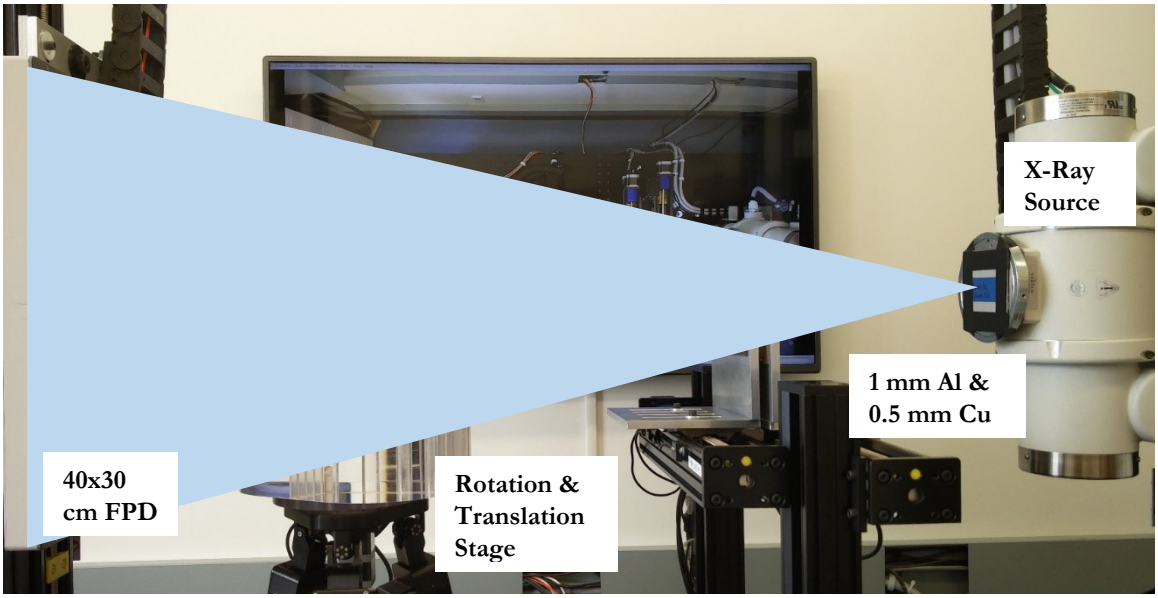

Figure 8. CBCT test bench used to obtain physical measurement data

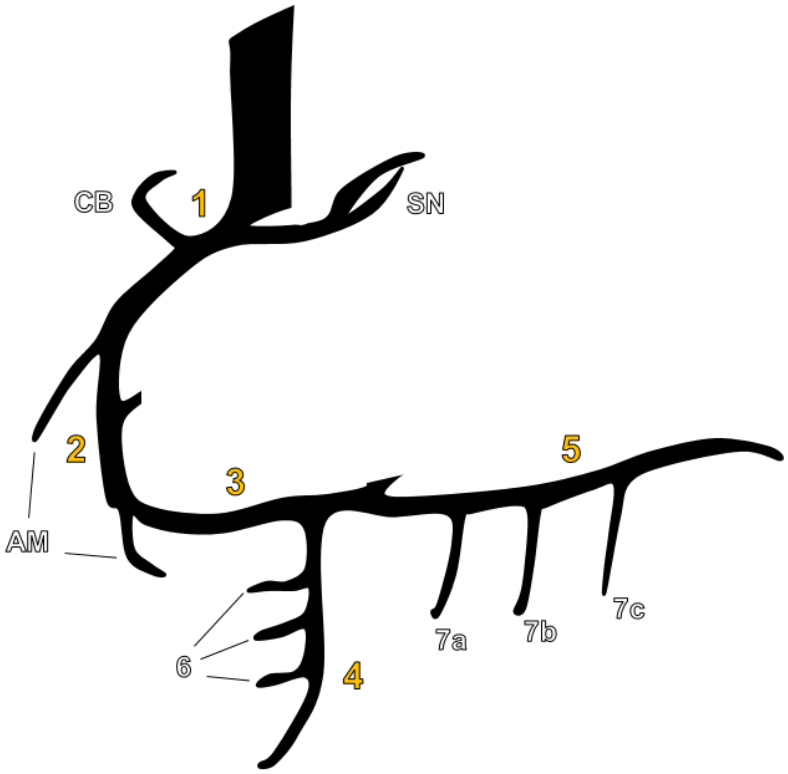

Segment	Map Location
1	Proximal right coronary artery conduit segment
2	Mid-right coronary artery conduit segment
3	Distal right coronary artery conduit segment
4	Right posterior descending artery segment
5	Right posterior AV segment
6	Posterior descending septal perforators segment(s)
7a	First right posterolateral segment
7b	Second right posterolateral segment
7c	Third right posterolateral segment

AM acute marginal segment(s), *CB* conus branch, *SN* sinus node artery, *AV* atrioventricular

Figure 9. Right coronary artery segments system according to ACC/AHA Guidelines for Coronary Angiography.

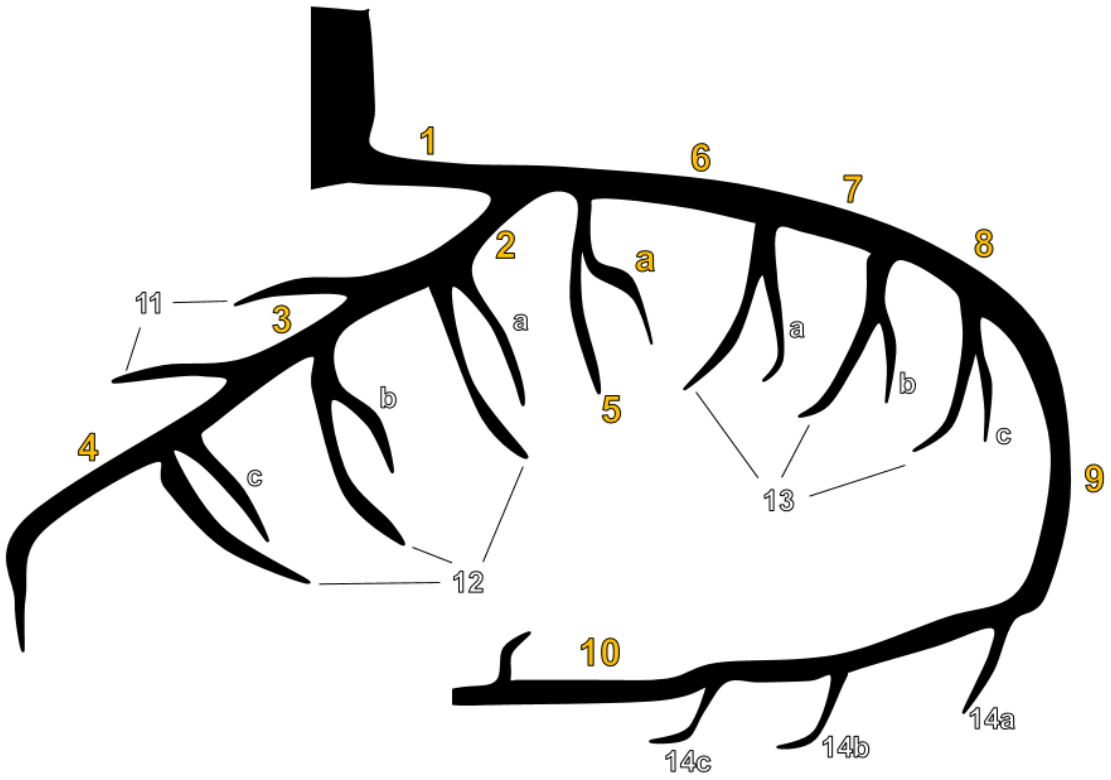

Segment	Map Location
1	Left main coronary artery segment
2	Proximal LAD artery segment
3	Mid-LAD artery segment
4	Distal LAD artery segment
5	Ramus intermedius segment
5a	Lateral ramus intermedius segment
11	LAD septal perforator segment(s)
12	Diagonal branch segment(s)
12a	Lateral first diagonal branch segment
12b	Lateral second diagonal branch segment
12c	Lateral third diagonal branch segment

LAD left anterior descending coronary artery branch

Figure 10. Left coronary artery segments system according to ACC/AHA Guidelines for Coronary Angiography

Segment	Map Location
6	Proximal circumflex artery segment
7	Mid-circumflex artery segment
8	Distal circumflex artery segment
9	Circumflex artery AV groove continuation segment
10	Left posterolateral descending artery segment
13	Obtuse marginal branch segment(s)
13a	Lateral first obtuse marginal branch segment
13b	Lateral second obtuse marginal branch segment
13c	Lateral third obtuse marginal branch segment
14a	First left posterolateral branch segment
14b	Second left posterolateral branch segment
14c	Third left posterolateral branch segment

30%				
point #	location	x	y	z
1	LCX_OM1	282.5	275.5	380.5
2	LCX_2ndPL	269.5	323.5	167.5
3	LM_LAD/LCX	262.5	260.5	366.5
4	2ndPL_L1	259.5	305.5	159.5
5	D1_L1	314.5	225.5	370.5
6	Ao	232.5	236.5	368.5
7	LCX_1stPDA/2ndPDA	262.5	319.5	146.5
8	LAD_D1	292.5	236.5	376.5
9	LAD_S2	329.5	130.5	254.5
10	LAD_S1	299.5	222.5	361.5
11	LCX_1stPL	272.5	325.5	173.5
12	LCX_OM3	296.5	342.5	222.5

Table 1. Slice locations of bifurcation points at various coronary artery segments (labeled) at the chosen end systolic phase.

75%				
point #	location	x	y	z
13	LCX_OM1	268.5	281.5	388.5
7	LCX_2ndPL	256.5	342.5	186.5
12	LM_LAD/LCX	257.5	270.5	383.5
17	D1_L1	311.5	234.5	386.5
1	Ao	229.5	251.5	377.5
5	LCX_1stPDA/2ndPDA	246.5	339.5	162.5
2	LAD_D1	291.5	243.5	389.5
4	LAD_S2	328.5	142.5	280.5
16	LAD_S1	298.5	229.5	371.5
6	LCX_1stPL	258.5	346.5	190.5
9	LCX_OM3	282.5	361.5	240.5

Table 2. Slice locations of bifurcation points at various coronary artery segments (labeled) at the chosen end diastolic phase.

location	x	y	z
LCX_OM1	14	-6	-8
LCX_2ndPL	13	-19	-19
LM_LAD/LCX	5	-10	-17
2ndPL_L1			
D1_L1	3	-9	-16
Ao	3	-15	-9
_1stPDA/2nd	16	-20	-16
LAD_D1	1	-7	-13
LAD_S2	1	-12	-26
LAD_S1	1	-7	-10
LCX_1stPL	14	-21	-17
LCX_OM3	14	-19	-18
-7	8	-13	-15

Table 3. Specific and average displacement of various coronary artery segments, estimated from the locations of corresponding bifurcation point at the end systolic and end diastolic phase.

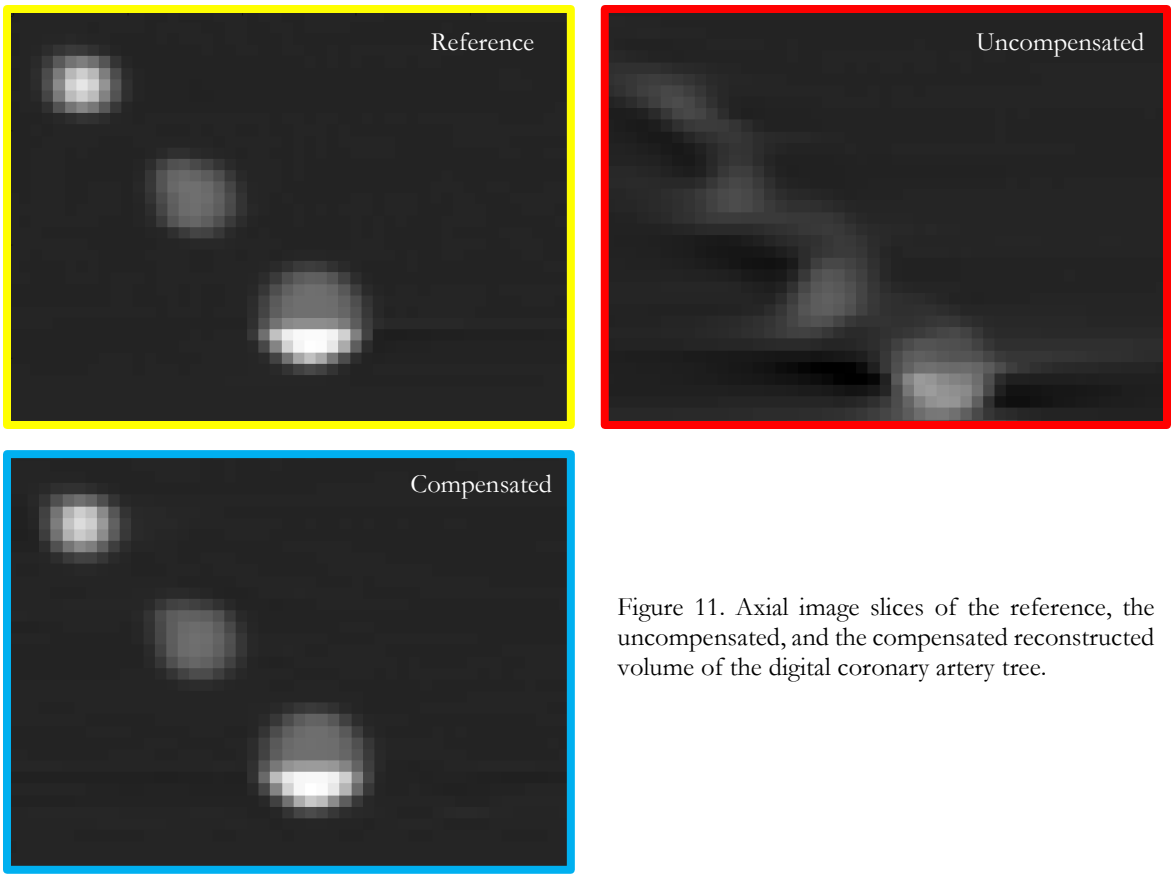

Figure 11. Axial image slices of the reference, the uncompensated, and the compensated reconstructed volume of the digital coronary artery tree.

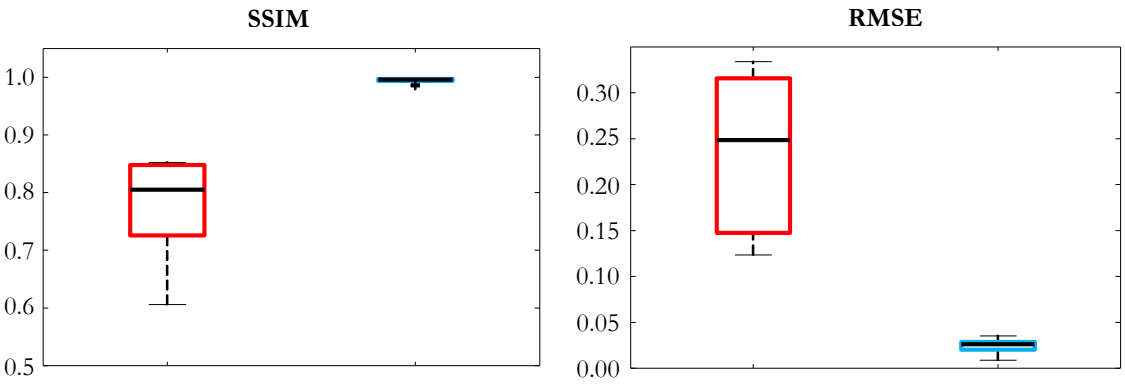

Figure 12. SSIM and RMSE values of the uncompensated (red) and the compensated (blue) volume.

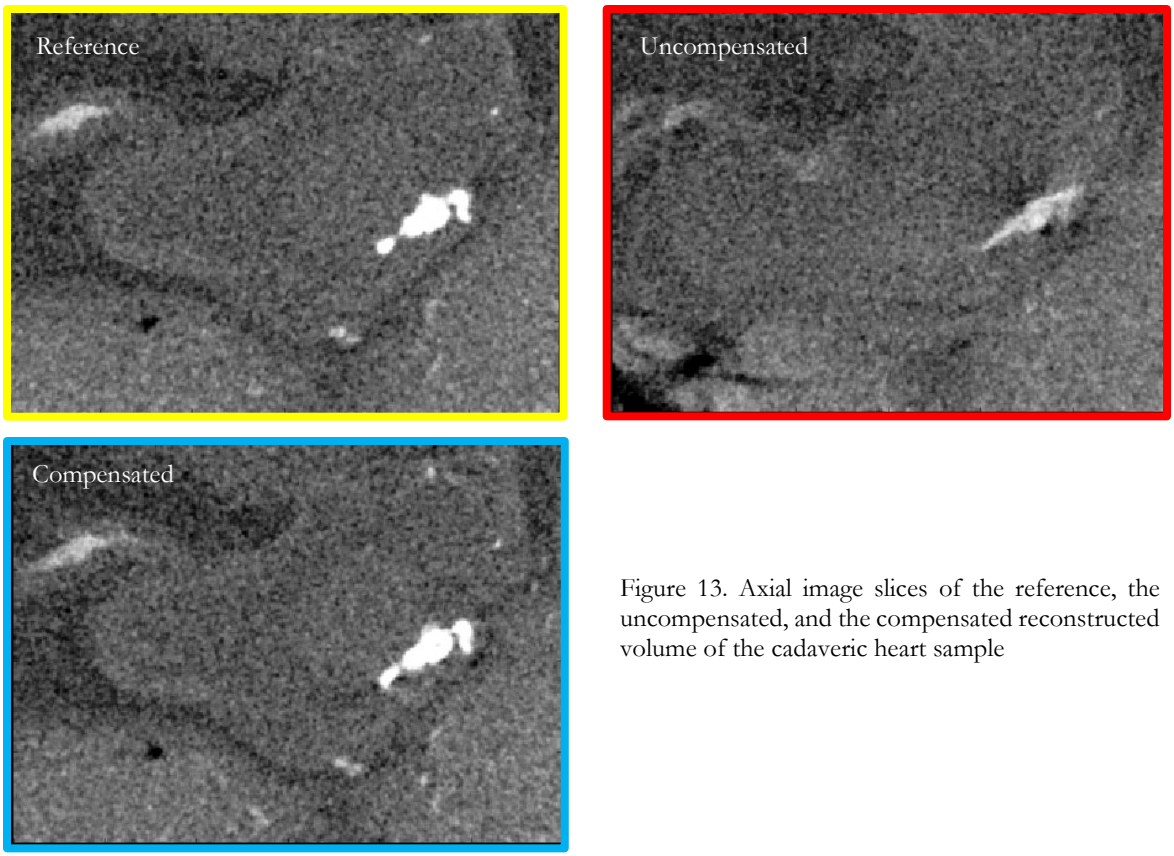

Figure 13. Axial image slices of the reference, the uncompensated, and the compensated reconstructed volume of the cadaveric heart sample

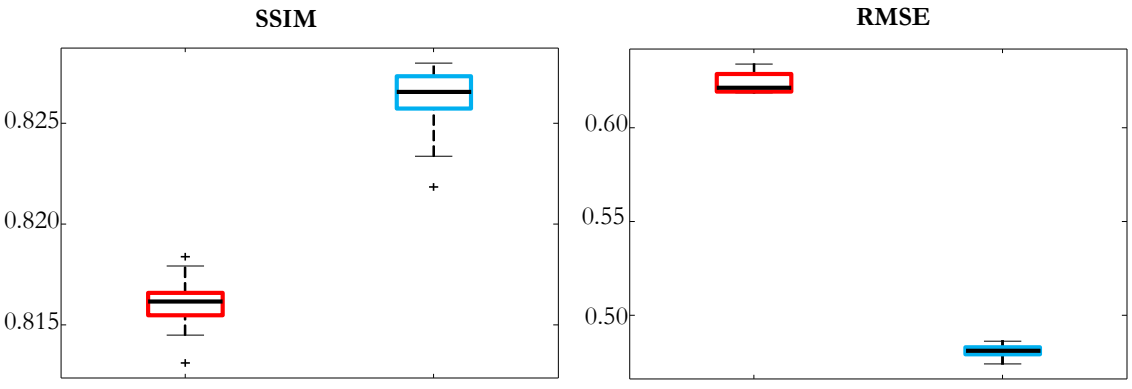

Figure 14. SSIM and RMSE values of the uncompensated (red) and the compensated (blue) volume.

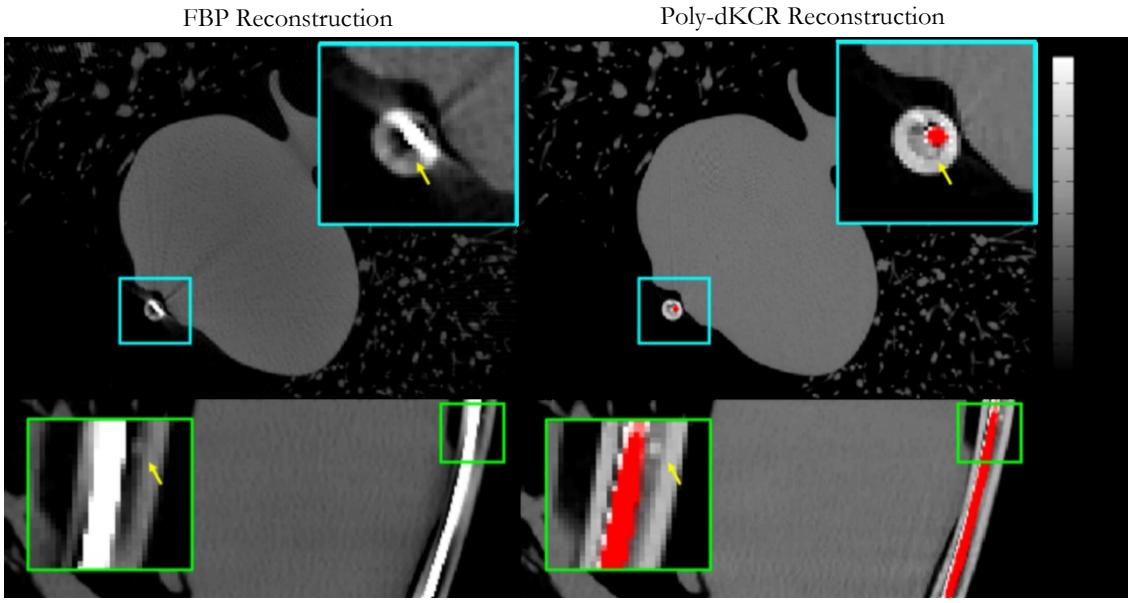

Figure 15. Performance assessment of the Poly-dKCR method.

Axial and sagittal views are shown for (A) the FBP reconstruction and (B) the Poly-dKCR volume. The Teflon sphere is indicated in each view by a yellow arrow.

Reference

[1] L. Husmann, S. Leschka, L. Desbiolles, T. Schepis, O. Gaemperli, B. Seifert, P. Cattin, T. Frauenfelder, T. G. Flohr, B. Marincek, P. a Kaufmann, and H. Alkadhi, "Coronary artery motion and cardiac phases: dependency on heart rate -- implications for CT image reconstruction.," *Radiology*, vol. 245, no. 2, pp. 567–576, 2007.

[2] T.-S. Pan and Y. Shen, "Phase-Driven Multisector Reconstruction for Multislice Helical CT Imaging," vol. US 6,504,8, 2003.

[3] T. G. Flohr, C. H. McCollough, H. Bruder, M. Petersilka, K. Gruber, C. Sub, M. Grasruck, K. Stierstorfer, B. Krauss, R. Raupach, A. N. Primak, A. Kuttner, S. Achenbach, C. Becker, A. Kopp, and B. M. Ohnesorge, "First performance evaluation of a dual-source CT (DSCT) system," *Eur. Radiol.*, vol. 16, no. 2, pp. 256–268, 2006.

[4] S. Achenbach, U. Ropers, A. Kuettner, K. Anders, T. Pflederer, S. Komatsu, W. Bautz, W. G. Daniel, and D. Ropers, "Randomized Comparison of 64-Slice Single- and Dual-Source Computed Tomography Coronary Angiography for the Detection of Coronary Artery Disease," *JACC Cardiovasc. Imaging*, vol. 1, no. 2, pp. 177–186, 2008.

[5] M. D. Shapiro, A. J. Pena, J. H. Nichols, S. Worrell, F. Bamberg, N. Dannemann, S. Abbara, R. C. Cury, T. J. Brady, and U. Hoffmann, "Efficacy of pre-scan beta-blockade and impact of heart rate on image quality in patients undergoing coronary multidetector computed tomography angiography," *Eur. J. Radiol.*, vol. 66, no. 1, pp. 37–41, 2008.

[6] M. Kachelrieß, S. Ulzheimer, and W. Kalender, "ECG-correlated image reconstruction from subsecond multi-slice spiral CT scans of the heart," *Med. Phys.*, vol. 27, no. 8, pp. 1881–1902, 2000.

[7] A. A. Zamyatin, B. S. S. Chiang, and S. Nakanishi, "Motion weighting in helical computed tomography with wide cone angle," *IEEE Nucl. Sci. Symp. Conf. Rec.*, vol. 60061, pp. 2860–2863, 2010.

[8] Q. Tang, J. Cammin, S. Srivastava, and K. Taguchi, "A fully four-dimensional, iterative motion estimation and compensation method for cardiac CT.," *Med. Phys.*, vol. 39, no. 7, pp. 4291–305, 2012.

[9] a a Isola, C. T. Metz, M. Schaap, S. Klein, W. J. Niessen, and M. Grass, "Coronary segmentation based motion corrected cardiac CT reconstruction," *IEEE Nucl. Sci. Symp. Med. Imaging Conf.*, pp. 2026–2029, 2010.

[10] J. Wicklein, G. Lauritsch, K. Müller, H. Kunze, W. Kalender, and Y. Kyriakou, "Aortic Root Motion Correction in C-Arm Flat-Detector CT," *Fully 3D Meet.*, 2013.

[11] A. Sisniega, J. W. Stayman, Q. Cao, J. Yorkston, J. H. Siewerdsen, and W. Zbijewski, "Motion Estimation Using a Penalized Image Sharpness Criterion for Resolution Recovery in Extremities Cone-Beam CT," *CT Meet.*, 2016.

[12] W. a Kalender, R. Hebel, and J. Ebersberger, "Reduction of CT artifacts caused by metallic implants.," *Radiology*, vol. 164, no. 2, pp. 576–577, 1987.

[13] O. Watzke and W. A. Kalender, "A pragmatic approach to metal artifact reduction in CT: Merging of metal artifact reduced images," *Eur. Radiol.*, vol. 14, no. 5, pp. 849–856, 2004.

[14] H. Li, L. Yu, X. Liu, and C. H. McCollough, "Metal artifact suppression from reformatted projections in multi-slice helical CT using dual-front active contours," *Proc. 31st Annu. Int. Conf. IEEE Eng. Med. Biol. Soc. Eng. Futur. Biomed. EMBC 2009*, vol. 5155, no. 2010, pp. 993–996, 2009.

[15] X. Duan, L. Zhang, Y. Xiao, J. Cheng, Z. Chen, and Y. Xing, "Metal artifact reduction in CT images sinogram TV inpainting," *IEEE Nucl. Sci. Symp. Conf. Rec.*, no. 3, pp. 4175–4177, 2008.

[16] Y. Zhang, Y. F. Pu, J. R. Hu, Y. Liu, and J. L. Zhou, "A new CT metal artifacts reduction algorithm based on fractional-order sinogram inpainting," *J. Xray. Sci. Technol.*, vol. 19, no. 3, pp. 373–384, 2011.

[17] M. Bal and L. Spies, "Metal artifact reduction in CT using tissue-class modeling and adaptive prefiltering.," *Med. Phys.*, vol. 33, no. 8, pp. 2852–2859, 2006.

[18] M. R. Paudel, M. Mackenzie, B. G. Fallone, and S. Rathee, "Clinical evaluation of normalized metal artifact reduction in kVCT using MVCT prior images (MVCT-NMAR) for radiation therapy treatment planning," *Int. J. Radiat. Oncol. Biol. Phys.*, vol. 89, no. 3, pp. 682–689, 2014.

[19] J. W. Stayman, Y. Otake, J. L. Prince, A. J. Khanna, and J. H. Siewerdsen, "Model-based tomographic reconstruction of objects containing known components," *IEEE Trans. Med. Imaging*, vol. 31, no. 10, pp. 1837–1848, 2012.

[20] J. W. Stayman, H. Dang, Y. Otake, W. Zbijewski, J. Noble, B. Dawant, R. Labadie, J. P. Carey, and J. H. Siewerdsen, "Overcoming Nonlinear Partial Volume Effects in Known-Component Reconstruction of Cochlear Implants.," *Proc. SPIE--the Int. Soc. Opt. Eng.*, vol. 8668, p. 86681L, 2013.

[21] J. W. Stayman, Y. Otake, S. Schafer, a. J. Khanna, J. L. Prince, J. H. Siewerdsen, S. Schafer, and a. J. Khanna, "Model-based reconstruction of objects with inexactly known components," *SPIE Med. Imaging 2012 Phys. Med. Imaging*, vol. 8313, no. 10, pp. 8313–1S, 2012.

[22] B. Lu, S. S. Mao, N. Zhuang, H. Bakhsheshi, H. Yamamoto, J. Takasu, S. C. Liu, and M. J. Budoff, "Coronary artery motion during the cardiac cycle and optimal ECG triggering for coronary artery imaging.," *Invest. Radiol.*, vol. 36, no. 5, pp. 250–256, 2001.

[23] O. Friman, C. Kuhnel, and H.-O. Peitgen, "Coronary centerline extraction using multiple hypothesis tracking and minimal paths," *Med. Image Comput. Comput. Interv.*, pp. 1–8, 2008.

[24] J. Hsieh, R. C. Molthen, C. a Dawson, and R. H. Johnson, "An iterative approach to the beam hardening correction in cone beam CT.," *Med. Phys.*, vol. 27, no. 1, pp. 23–29, 2000.

[25] H. Erdogan and J. A. Fessler, "Ordered subsets algorithms for transmission tomography," *Phys. Med. Biol.*, vol. 44, no. 11, pp. 2835–2851, 1999.

[26] A. S. Wang, J. W. Stayman, Y. Otake, G. Kleinszig, S. Vogt, G. L. Gallia, A. J. Khanna, and J. H. Siewerdsen, "Soft-tissue imaging with C-arm cone-beam CT using statistical reconstruction.," *Phys. Med. Biol.*, vol. 59, no. 4, pp. 1005–26, 2014.

[27] J. W. Stayman, S. Tilley, and J. H. Siewerdsen, "Integration of Component Knowledge in Penalized-Likelihood Reconstruction with Morphological and Spectral Uncertainties.," *Conf. Proc. / Int. Conf. Image Form. X-Ray Comput. Tomogr.*, vol. 2014, pp. 111–115, 2014.

[28] N. Otsu, "A threshold selection method from gray-level histograms," *IEEE Trans. Syst. Man. Cybern.*, vol. 9, no. 1, pp. 62–66, 1979.

[29] Y. Otake, A. S. Wang, J. Webster Stayman, A. Uneri, G. Kleinszig, S. Vogt, A. J. Khanna, Z. L. Gokaslan, and J. H. Siewerdsen, "Robust 3D-2D image registration: application to spine interventions and vertebral labeling in the presence of anatomical deformation.," *Phys. Med. Biol.*, vol. 58, no. 23, pp. 8535–53, 2013.

[30] A. Uneri, J. W. Stayman, T. De Silva, A. S. Wang, G. Kleinszig, S. Vogt, J.-P. Wolinsky, Z. L. Gokaslan, and J. H. Siewerdsen, "Known-component 3D-2D registration for image guidance and quality assurance in spine surgery pedicle screw placement," *SPIE Med. Imaging*, vol. 9415, no. 443, pp. 1–7, 2015.

[31] P. J. Scanlon, D. P. Faxon, A. Audet, B. Carabello, J. Gregory, K. A. Eagle, R. D. Legako, D. F. Leon, J. A. Murray, E. Nissen, C. J. Pepine, R. M. Watson, J. L. Ritchie, R. J. Gibbons, M. D. Cheitlin, T. J. Gardner, A. Garson, O. Richard, T. J. Ryan, and S. C. Smith, *ACC / AHA PRACTICE GUIDELINES ACC / AHA Guidelines for Coronary Angiography*, vol. 33, no. 6. 1999.

[32] Z. Wang, A. C. Bovik, and H. R. Sheikh, "Image quality assessment: From error measurement to structural similarity," *IEEE Trans. image*, vol. 13, no. 1, pp. 1–14, 2004.

XIAOXUAN ZHANG

2 W University Pkwy #403, Baltimore, MD 21218

Email: xiaoxuanzhang9@gmail.com Phone: 949-861-0413

EDUCATION

Johns Hopkins University

Master of Science and Engineering in Biomedical Engineering (expect July 2016)

University of California, Irvine

Bachelor of Science in Biomedical Engineering (June 2014)

ENGINEERING PROJECTS

Coronary Artery Motion Estimation and Compensation August 2014 – Present

Independent study | Graduate Research Assistant *Baltimore, MD*

- Quantify coronary artery motion on cardiac image volumes reconstructed from 2D patient data
- Generate and integrate a motion model into a state-of-art iterative compensation framework
- Program and induce movement of an explanted heart via a MATLAB-controlled platform
- Verify the effectiveness of the motion model with both simulation and ex vivo experiments
- Deliver up to 60% increase in image similarity between the compensated data and the ground truth
- Abstract submission to the 2016 American Association of Physicists in Medicine accepted as an oral presentation

Biomedical Engineering Senior Design September 2013 – June 2014

Co-inventor of Patent PCT/US2014/066558 *Irvine, CA*

- Developed an enhanced breast biopsy guidewire in collaboration with senior breast surgeons

- Investigated a wide range of novel lesion localization markers for ultrasound and mammography
- Fabricated functional guidewire prototype assemblies for demonstration and initial testing
- Prepared essential documents and created invention illustrations for provisional patent application

Transmittance Pulse Oximeter Design September – December 2013

Class project | Team Member (group of 2) *Irvine, CA*

- Measured arterial oxygen saturation by monitoring the variation in tissue light absorbance
- Built an Arduino-based sensor system to enable light emission and transmitted data acquisition
- Enhanced signal peak-valley detection by reducing noisy waveforms with LabVIEW
- Achieved comparable measurement accuracy to a commercial pulse oximeter

Biomedical Engineering Practice and Innovation June – August 2015

Summer part-time | Teaching Assistant *Baltimore, MD*

- Acquired and analyzed electrocardiogram (ECG) data in different body positions with Biopac
- Described the limitations of conventional imaging techniques in cardiac catheterization
- Explain the etiology of common Doppler Ultrasound artifacts and collect image samples
- Designed and constructed ultrasound phantoms with pulsating simulated blood flow

LANGUAGES

Proficient: Python, MATLAB

Previously used: LabVIEW, C

SOFTWARE APPLICATIONS

Git, OsiriX, MeVisLab, ImageJ